small methods
www.small-methods.com

In Situ Solution-Processed Submicron Thick SiO_xC_y/a-SiN_x(O):H Composite Barrier Film for Polymer:Non-Fullerene Photovoltaics

Jian Qin, Na Wu, Wei Chen, Bowen Liu, Zhenguo Wang, Lianping Zhang, Ni Yin, Qi Chen, Zong-Bo Zhang,* and Chang-Qi Ma**

Aiming to improve the environmental stability of organic photovoltaics, a multilayered SiO_xC_y/a-SiN_x(O):H composite barrier film coated with a hydrophobic perfluoro copolymer stop layer for polymer:non-fullerene solar cells is developed. The composite film is prepared by spin-coating of polysilicone and perhydropolysilazane (PHPS) following a densification process by vacuum ultraviolet irradiation in an inert atmosphere. The transformation of polysilicone and PHPS to SiO_xC_y and a-SiN_x(O):H is confirmed by Fourier transform infrared and energy-dispersive X-ray spectroscopy measurement. However, the as-prepared PHPS-derived silicon nitride (PDSN) can react with moisture in the ambient atmosphere, yielding microscale defects and a consequent poor barrier performance. Treating the incomplete PDSN with methanol vapor significantly densifies the film yielding low water vapor transmission rates (WVTRs)of 5.0×10^{-1} and 2.0×10^{-1} g m^{-2} d^{-1} for the one- and three-couple of SiO_xC_y/a-SiN_x(O):H (CON) composite films, respectively. By incorporating a thin hydrophobic perfluoro copolymer layer, the three-coupled methanol-treated CON film with a total thickness of 600 nm shows an extremely low WVTR of 8.7×10^{-4} g m^{-2} d^{-1}. No performance decay is measured for the PM6:Y6 and PM6:L8-BO cells after such an encapsulation process. These encapsulated polymer cells show good stability storaged at 25 °C/50% relative humidity, or under simulated extreme rainstorm tests.

1. Introduction

Energy consumption and climate change are the two major concerns confronting humanity in the 21st century.[1,2]One key strategy for addressing these issues is the development of new energy sources and technologies.[3–6] Over the past decades, photovoltaic—a method that can directly convert solar energy to electricity—has been recognized as the most important renewable energy source.[7,8] Organic photovoltaics (OPVs) that are based on organic semiconductors with multiple nano-thin films received much attention owing to their nature of light weight, flexibility, transparency, and colorfulness.[9–13] More importantly, OPVs can be prepared by roll-to-roll printing processes, enabling mass production and low-cost potentials.[10,14] With the development of material and device engineering, the power conversion efficiency (PCE) of OPVs has increased to more than 19%,[15–17] reaching the threshold of commercial application. However, the environmental instability of OPVs has

J. Qin, W. Chen, B. Liu, Z. Wang, Q. Chen, C.-Q. Ma
School of Nano-Tech and Nano-Bionics
University of Science and Technology of China
Hefei 230027, P. R. China
E-mail: cqma2011@sinano.ac.cn

J. Qin, N. Wu, W. Chen, B. Liu, Z. Wang, L. Zhang, N. Yin, Q. Chen, C.-Q. Ma
i-Lab, Suzhou Institute of Nano-Tech and Nano-Bionics
Chinese Academy of Sciences
Suzhou 215123, P. R. China
E-mail: nwu2022@sinano.ac.cn

J. Qin, N. Wu, W. Chen, B. Liu, Z. Wang, C.-Q. Ma
Printable Electronics Research Center & i-Lab, Suzhou Institute of Nano-Tech and Nano-Bionics
Chinese Academy of Sciences
Suzhou 215123, P. R. China

Z.-B. Zhang
Key Laboratory of Science and Technology on High-tech Polymer Materials
Institute of Chemistry
Chinese Academy of Sciences
Beijing 100190, P. R. China
E-mail: zongbo@iccas.ac.cn

The ORCID identification number(s) for the author(s) of this article can be found under https://doi.org/10.1002/smtd.202300224

DOI: 10.1002/smtd.202300224

become the most crucial obstacle limiting their commercialization, where damages to the electrodes, the interfacial layers, and the interior components by water and oxygen are the external issues.[18–21] Although there are numerous studies dedicated to developing more stable materials,[22,23] electrodes,[24,25] and interfaces[26,27] to improve OPVs' environmental stability, the long-term stability of OPVs is still far from satisfactory for practical applications. A barrier film that can effectively block the contact between water/oxygen and organic solar cells is essential for achieving high environmental stability of OPVs.[19,28,29]

Currently, most OPVs adopt cover encapsulation, where the cover slide is attached to the cell through ultraviolet (UV) or thermal curable epoxy and acrylic sealant.[30] However, using high-barrier slides dramatically increases the overall weight and cost of the cells. Also, UV- or heat-curing adhesives may cause damage to device performance during the curing process. Furthermore, edge penetration of water and/or oxygen between the cover and the cell has not been effectively resolved, and the delamination of the barrier film may cause devastating damage to the device.[31,32] Thin film encapsulation (TFE) is an alternative method to cover-to-cell encapsulation, where the multilayered organic/inorganic barrier film is deposited directly on the device.[33,34] TFE is expected to reduce the weight and cost of polymer solar cells, enable excellent flexibility, and more importantly, to block the edge penetration of the water/oxygen effectively. In the multiple organic-inorganic stacked barrier thin films, the inorganic layer functions as the key layer to block the penetration of water/oxygen molecules, whereas the organic layer offers excellent flexibility to minimize the interface stress and passivate the defects of the inorganic layer.[33–35] Until now, most inorganic layers were prepared by vacuum-based thin film deposition methods, including Chemical Vapor Deposition (CVD),[36] Atomic Layer Deposition (ALD),[37] etc. However, the harsh deposition conditions might cause damage to OPVs, making the vacuum-based TFE method not ideal for OPVs.[32,35] A new mild method for preparing TFE is highly needed for OPVs.

Polymer-derived ceramic (PDC) is a new approach to achieve nanometer ceramic thin film by converting solution-processable preceramic polymers with pyrolysis[38] or UV light irradiation.[39] Since most organic electronics are not compatible with high-temperature pyrolysis, UV light assistant conversion of preceramic polymers is the most feasible way for preparing inorganic thin barrier films.[39–43] Among various preceramic polymers, perhydropolysilazane (PHPS) is the most widely used PDC material since it can be converted to SiO_x or SiN_x thin films under mild conditions. For example, Prager et al. reported the conversion of PHPS to a SiO_x network triggered by vacuum ultraviolet (VUV, $\lambda = 172$ nm) irradiation, which is ascribed to the Si-N scission with VUV light excitation.[44] A high barrier improvement factor (BIF) of 400 was achieved for the PHPS-derived SiO_x (PDSO) coated PET film. Similarly, Kobayashi et al. reported the conversion of PHPS to silica with VUV light, and a low WVTR of 10^{-1} to 10^{0} g m^{-2} d^{-1} was achieved.[41] Following this, Channa et al. reported the preparation of SiO_x thin films by converting PHPS under VUV irradiation for P3HT:PC_{61}BM OPVs in situ encapsulation.[45] In combination with a polyacrylic layer, multilayered barrier films were successfully prepared, which showed a low water vapor transmission rate (WVTR) of $<10^{-2}$ g m^{-2} d^{-1} (40 °C/85% relative humidity (RH)) and excellent flexibility. Knowing that conversion PDSO is usually performed in air that might cause the damage of solar cell performance, in situ preparation of silica nitride as the barrier layer was then developed since PHPS can be also derived to silicon nitride (PDSN) in N_2 atmosphere.[42] Sun et al. reported the preparation of PDMS/SiO_x/SiN_y/SiO_xN_y organic/inorganic multilayer for in situ encapsulation of OLEDs, where the PDMS was converted to SiO_x and PHPS thin film was converted to SiN_x in N_2-filled glovebox by 172 nm VUV irradiation.[46] The PDMS and PDSN serve as the organic and inorganic layers, respectively. A three-coupled PDMS/SiO_x/SiN_y/SiO_xN_y organic/inorganic thin film showed a low WVTR$< 10^{-4}$ gm^{-2}d^{-1}, which is close to a level of barrier performance of conventional glass cover encapsulation.[46]

In this work, we report the preparation of multilayered SiO_xC_y/a-SiN_x(O):H films from silicone and PHPS directly in a N_2-filled glovebox by 172 nm VUV irradiation. Preparation of the barrier films in an N_2-filled glovebox can prevent severe damage by water/oxygen and atomic oxygen generated by VUV irradiation. However, the conversion of PHPS to a-SiN_x(O):H film is not complete, which would further hydrolyze in the air, yielding micron scale defects within the film. We then developed a methanol vapor treatment to release unconverted chemical bonds within the nano-thin film to solve this problem. A three-stacked layer of SiO_xC_y/a-SiN_x(O):H showed a WVTR of 2×10^{-1} g m^{-2} d^{-1}. By cooperating with a hydrophobic perfluoro polymer named perfluoro(1-butenyl vinyl ether) (CYTOP) as the top stopping layer, a low WVTR of 8.7×10^{-4} g m^{-2} d^{-1} was obtained, which is sufficient for in situ OPVs encapsulation.[47,48] We then showed the use of this in situ prepared barrier films in high-performance polymer:non-fullerene solar cells against moisture (25 °C/50% RH) and extreme rainstorm (50 mm h^{-1}) for the first time, proving a high reliability of the multilayered barrier films.

2. Results and Discussion

2.1. VUV-Assisted Polymer Derived SiO_xC_y/SiN_x(O):H Stacked Multilayers

Figure 1a depicts the deposition processes for the multilayer silicone/PHPS thin film. The silicone copolymer layer was prepared by spin coating a mixture of precursors (Shin-Etsu KER 4690-A and B, in a weight ratio of 1:1) in decamethylcyclopentasiloxane onto the substrate and the follow-up polymerization initiated with VUV light ($\lambda = 172$ nm). It is worth noting that illumination the silicone layer with UV light of 356 nm or 254 nm was unable to polymerize the silicone film, yielding a viscous thin film and making this not suitable for the deposition of PHPS layer. After the solidification of polysilicone layer, PHPS was deposited via spin coating on the surface and then converted to the amorphous silicon nitride with 172 nm VUV irradiation. The multilayered structure was achieved by repeating silicone polymerization and PHPS conversion processes. Figure 1c shows the correlation of the chemical bonding energy to the wavelength of light. As seen here, UV light with a wavelength of 172 nm has a high energy of 692 KJ mol^{-1}, which is much higher than the bonding energy of Si-C (318 KJ mol^{-1}), Si-O (452 KJ mol^{-1}), Si-N (355 KJ mol^{-1}), N-H (386 KJ mol^{-1}) and Si-H (318 KJ mol^{-1}), indicating that 172 nm VUV light could break and rearrange these chemical

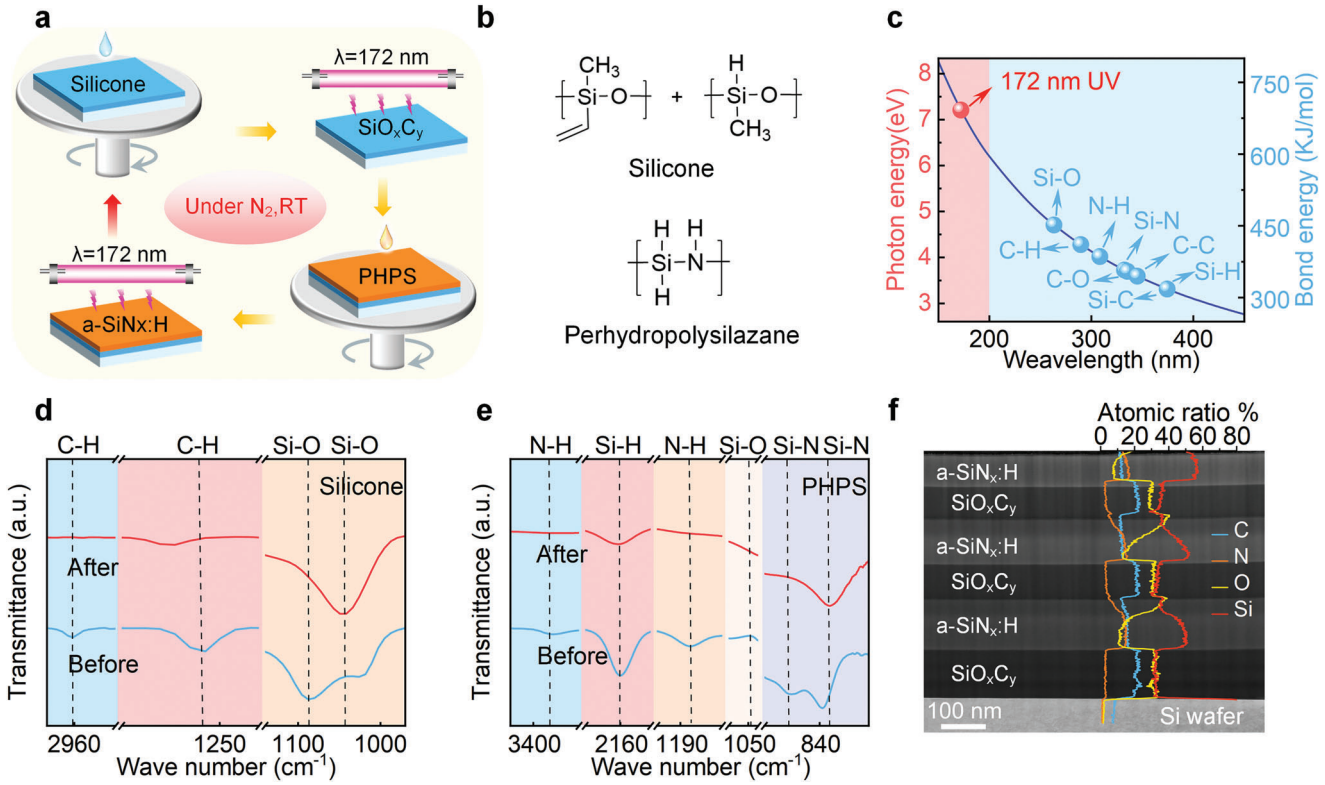

Figure 1. Preparation of SiO_xC_y/a-SiN_x(O):H multilayer barrier film. a) Process for the deposition of the multilayered SiO_xC_y/a-SiN_x(O):H barrier film by solution process. b) The molecular formula of silicone and perhydropolysilazane. c) Comparison of bond energy in silicone and PHPS with photon energy of 172 nm VUV light. d) FTIR spectra of silicone before (blue line) and after (red line) VUV treatment (20 min). e) FTIR spectra of PHPS before (blue line) and after (red line) VUV treatment (1 h). f) Cross-sectional TEM images and EDS of triple CON coatings on silicon wafers by in-situ solution process.

bonds in silicone and PHPS. In a recent study by Sasaki et al. demonstrated that the use of high intensity VUV source can significantly accelerate the conversion process, which opens up possibilities for industrial applications.[49] The VUV assisted conversion mechanism of the silicone and PHPS was then characterized by fourier transform infrared (FTIR). Figure 1d shows the FTIR spectra of the silicone film deposited on CaF_2 slides before and after VUV light irradiation. Figure S1 in supporting information shows the evolution of the FTIR spectrum of the silicone film upon VUV irradiation over 20 min. As seen from these FTIR spectra, the symmetric stretching vibration (2960–2980 cm^{-1}) and bending vibration (1250–1280 cm^{-1}) of the C-H bonds[50] get weaker after VUV irradiation, whereas the symmetric stretching vibration of the Si-O bond (1000–1100 cm^{-1}) was enhanced upon VUV curing, indicating the formation of cross-linked O-Si-O bonds by breaking C-H bonds and rearranging the Si-O-Si chain of the silicone. Similarly, the stretching vibration signals of Si-H (2161 cm^{-1}) and N-H (3377 cm^{-1}) decreased significantly after 60 min of VUV irradiation inside the glovebox for PHPS film, whereas the Si-N signal of PHPS at 890 cm^{-1} disappeared and the Si-N signal at 835 cm^{-1} shifted to 823 cm^{-1} after VUV irradiation, indicating the formation of silicon nitride film through breaking the Si-H and N-H bonds and the following-up Si-N rearrangement (Figure 1e).[46,51,52] The densification of PHPS by hydrogen release and Si-N bond rearrangement is consistent with Sasaki's study.[51] In addition, the signal at 1047 cm^{-1} for the asymmetric stretching vibration of Si-O bond was slightly enhanced after VUV irradiation, indicating the formation of SiN_xO_y film as will be supported by energy-dispersive X-ray spectroscopy (EDS) results (vide infra).

The structure and composition of the multilayered thin film were characterized by transmission electron microscopy (TEM). A three-coupled thin film was prepared on a silicon wafer according to the method described above, and a cross-section sample was prepared by a focused ion beam (FIB). The prepared sample was then examined using TEM and the result is shown in Figure 1f. A multilayered structure with a clear boundary for each layer can be identified here. There are no evident penetration faults, indicating the excellent attachment of each layer during solution deposition and VUV conversion. The EDS corresponding to the TEM cross-sectional view shows that the deposited silicone contains mainly Si, C, and O, indicating the formation of SiO_xC_y composite under VUV irradiation. The layer thickness was measured to be ≈100 nm. On the other hand, the PHPS-converted layer contains mainly Si, N with a low concentration of O and C, similar to that reported by Sun et al.[50] Interestingly, significantly increased O concentration on the surface of the PHPS-derived silicon nitride (PDSN) film was measured, corresponding to the increased Si-O bonding depicted in Figure 1e. The oxygen element may come from residual oxygen in the glovebox, or from the residual solvent during the deposition. It is worth noting that the Si-H bonds exist in the converted film as confirmed in the

FTIR spectrum. With these, the inorganic layer generated following VUV irradiation of PHPS can be described as: a-SiN_x(O):H. The layer thickness was measured to be ≈100 nm as well. Eventually, a barrier film with three coupled alternating structure of SiO_xC_y/a-SiN_x(O):H (shorted as CON) was successfully obtained by full solution deposition with the assistance of VUV irradiation.

2.2. Synergistic Effects of Defects Engineering and Surface Protection to Improve Gas Barrier Performance

We then test the gas barrier performance of the solution-processed CON films using a calcium optical test method, which is based on the fact that the opaque calcium film turns transparent after forming $Ca(OH)_2$ and/or CaO by reacting with water or oxygen molecules. The rate of calcium area decrease is directly correlated to the water vapor transmission rate (WVTR) of barrier films according to the following equation:[54]

$$\mathrm{WVTR}\left(\mathrm{gm^{-2}day^{-1}}\right) = \mathrm{n} \times \delta_{\mathrm{Ca}} \times \frac{\mathrm{M}\left(\mathrm{H_2O}\right)}{\mathrm{M}\left(\mathrm{Ca}\right)} \times \mathrm{h} \times \frac{\mathrm{dA}}{\mathrm{dt}} \times \frac{1}{\mathrm{A}} \quad (1)$$

where n is the molar ratio of water to calcium in the calcium oxidation reaction and here n = 2, δ_{Ca} is the calcium density (1.55 g cm^{-3}), M(H_2O) and M(Ca) are the molar masses of water and calcium, respectively, h is the calcium thickness, dA/dt is the change rate of calcium area, and A is the area of evaporated calcium. The last term is entirely a scaling factor that connects the change in area of evaporated calcium to the comparable change in area of 1 m^2.[54] **Figure 2**a shows the photographs of the calcium film (50 nm thick) covered with different CON barrier films upon aging at 25 °C/100% RH in a climate chamber. In these figures, the optical contrast of the opaque calcium and the transparent $Ca(OH)_2$ area was enlarged to better show the calcium film's corrosion. The residual calcium area was calculated using the Java-based image conversion software ImageJ.[55] The corrosion rate of the calcium area can be derived from the curve of residual calcium area versus time (Figure 2b), and the WVTR of the barrier films (Figure 2c) was calculated according to Equation 1. As seen here, the calcium film was quickly corroded within one hour with one CON protection layer (the first row in Figure 2a), corresponding to a high WVTR of 2.5 g m^{-2} d^{-1}. With the increase in the layer stacking to three couples (the third row in Figure 2a), corrosion of calcium film was slowed down, yielding a WVTR of 5.5×10^{-1} g m^{-2} d^{-1}. The value of this WVTR is much higher than that reported in literature.[46] Apart from the differences of testing methods and conditions, the main reason is the presence of incomplete conversion of PHPS (vide infra). Figure 2d shows the surface morphology of the PDSN[51] film deposited on a silicon wafer measured by atomic force microscope (AFM) in air. Although a smooth surface could be measured at a small range of 2 μm × 2 μm (Figure S2a, Supporting Information), in addition to the nanometer scale small voids (< 0.5 μm), large volcano-like voids > 0.5 μm in diameter were measured of the film with a high defect density of 1.5×10^7/cm^2 on a larger range of 10 μm × 10 μm. To avoid the unexpected influence of ambient air, we measured the surface morphology of the PDSN film by AFM in a N_2-filled glove box. Figure S3a (Supporting Information) shows the result that nanoscale small voids were also formed, which was then ascribed to the evaporation of solvents and release of hydrogen during the densification of the PHPS film.[56] However, the voids with a scale of 0.5 μm or more were only found on the PHPS film measured in the air, indicating that such larger voids should be due to the interaction of the PHPS films with ambient air. Knowing that PHPS has a high reactivity with moisture, we speculate that the incomplete conversion of the PHPS film in N_2 atmosphere under VUV irradiation leads to a violent reaction with moisture in ambient air, causing the formation of voids. The reaction of incompletely converted PDSN with moisture was also confirmed by the rapid increase of defects on the surface of PDSN films within 60 min in air by 3D microscopy (Figure S4a,b, Supporting Information) and by the change of FTIR spectra of PDSN films within 60 min in air. (Figure S5, Supporting Information).

To minimize this unexpected effect, we perform a methanol vapor treatment on the VUV-converted film before transferring it to the air. Methanol was chosen as the solvent because of its lower reactivity than water vapor, so it could offer a mild conversion of PHPS to a more condensed SiN_x film. Figure 2e shows the AFM surface morphology of the MeOH vapor-treated PDSN film measured in air. As demonstrated here, the MeOH vapor-treated PDSN film in air showed a smooth surface without large void (> 0.5 μm), suggesting that MeOH treatment could significantly densify the silicon nitride layer. However, small voids that originates from the evaporation of solvents and the release of hydrogen are also found for the MeOH-treated film (vide supra), indicating that methanol treatment as a post-treatment process cannot fully eliminate the small voids. But the MeOH-process can prevent further enlargement of the film defects in air due to incomplete conversion and further reaction with humidity. The smoothing effect of methanol vapor on the PDSN film was also supported by a color 3D laser scanning microscope (CLSM) and Scanning Electron Microscope (SEM) measurements (Figure S6, Supporting Information). Similarly, a stable morphology of the MeOH-treated PDSN film in air was observed by 3D microscopy (Figure S4c,d, Supporting Information). To confirm the reaction between the PHPS and MeOH, FTIR of the PHPS film upon MeOH vapor treatment was measured and the results are shown in Figure 2f and Figure S7 (Supporting Information). As seen here, the Si-N signal of PHPS at 890 and 835 cm^{-1} vanished and the Si-O signal at 1072 cm^{-1} increased upon MeOH vapor treatment, indicating the reaction of PHPS with MeOH. Similarly, treating the PDSN film with MeOH vapor decreases the Si-N signal in the FTIR spectrum (Figure 2f), indicating that the PDSN can still react with methanol through the unconverted Si-N bonds. The hydrolysis of the Si-N bonds in the PDSN films is therefore ascribed to the main reason for the formation of microscale defects in the films when it is exposed to the air. On the other hand, the MeOH vapor treatment completes the conversion reaction of Si-N bonds and therefore passivates the formation of microscale defect. A densification mechanism for the MeOH vapor treatment is then illustrated in Figure 2j. Calcium test results also show improved water vapor barrier performance, where the methanol vapor treated one- and three-coupled CON films showed WVTR of 5×10^{-1} and 2×10^{-1} g m^{-2} d^{-1}, respectively, which is 1/5 and 1/3 of the untreated films (Figure 2c).

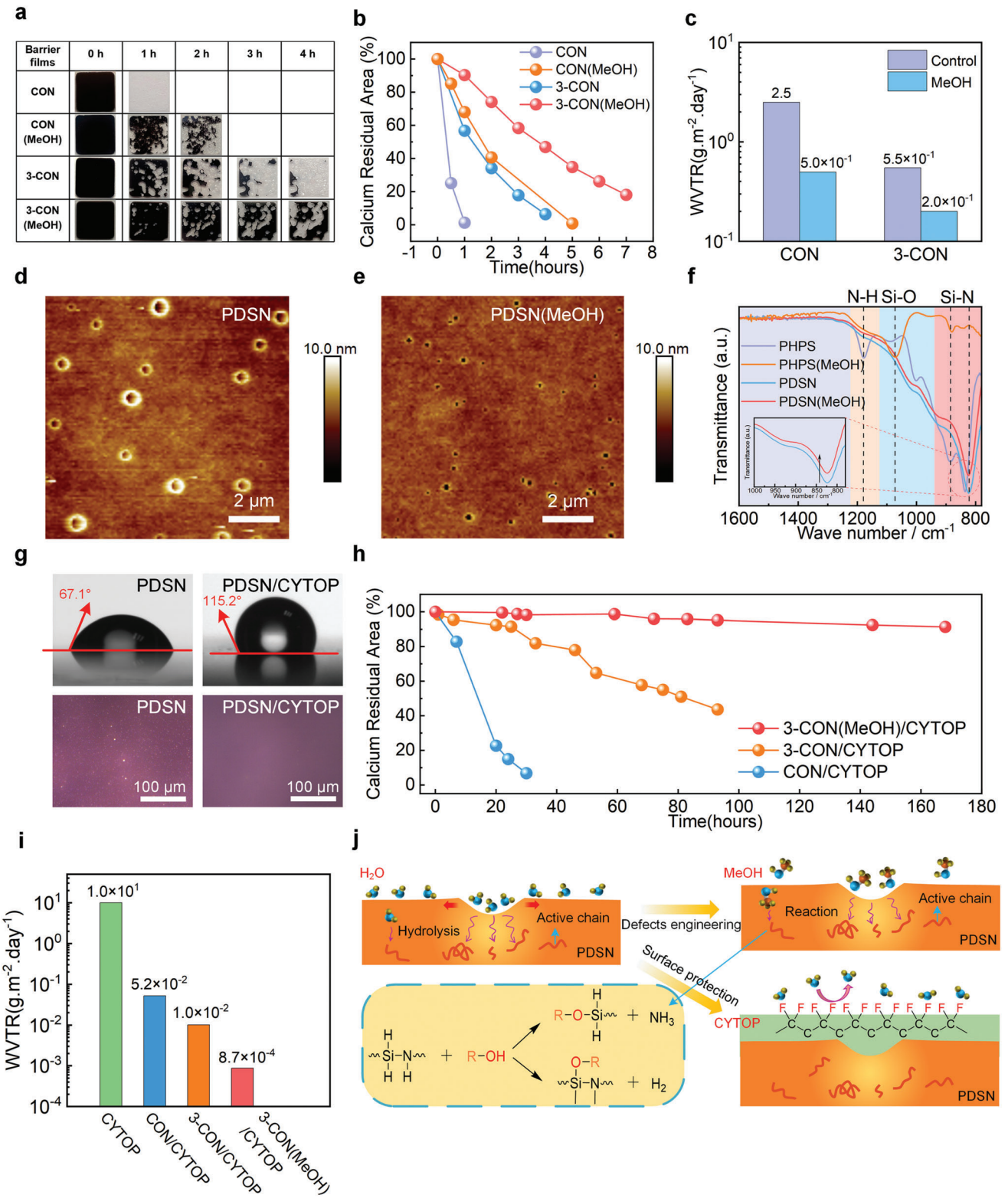

Figure 2. Characterization of the water vapor barrier performance of the multilayered CON films. a) Photographs of encapsulated calcium films aged at 25 °C/100% RH; b) The residue calcium area versus aging time of the calcium film covered with different barrier films; c) WVTR of different CON films with or without MeOH vapor treatment; d,e) AFM images of the as-prepared PDSN (d) and MeOH vapor treated PDSN (e) films measured in air; f) FTIR spectra of PHPS and the as-prepared PDSN films upon MeOH vapor treatment; g) Contact angles and 3D microscope measurement on the PDSN film with and without CYTOP cover layer; h) Evolution of the residue calcium area of calcium films covered with different barrier films; i) WVTR comparison on different barrier layers; j) Defect formation and CYTOP protection mechanism for the multiple layered barrier films.

We then tested the water vapor barrier effect of CON composite films for polymer solar cells. Polymer solar cells based on PM6:Y6 were fabricated. The cells were aged at 25 °C/50% RH in a climate chamber, and the devices' performance were checked. Figure S8 (Supporting Information) shows the evolution of device performance over aging time. As seen here, the performance of the cells decreases to 90% of its initial performance, which is much faster than that kept in glovebox. Further aging of the cell to 200 h yields a complete failure of the cells, similar to that observed in the encapsulated OLEDs.[57] These results indicate that, although WVTR of the MeOH-treated CON films was significantly reduced, the CON films are still not good enough for TFE for OPVs. A detailed inspection on the cells aged for 200 h showed obvious bumps of the electrode (Figure S8c,d, Supporting Information). A mechanism that the accumulation of water vapor at the CON film causes the shrinking of the barrier film that peels the MoO_3/Al electrode from the photoactive layer (Figure S8b, Supporting Information).

We checked the surface energy of the VUV converted PDSN surface. Figure 2g shows the photograph of a water droplet on the PDSN surface, from which a contact angle of 67.1° was measured, indicating a hydrophilic surface of PDSN film, which could be due to the formation of Si-O-H surface after VUV treatment and the consistent existence of defects. Considering that a hydrophilic surface would attract moisture, we think turning the hydrophilic surface to hydrophobic would help achieve a better WVTR. Therefore, a hydrophobic perfluoro polymer CYTOP was introduced to modify the PDSN surface. After such a surface modification, a high contact angle of 115.2° was obtained on the PDSN/CYTOP surface, and the filling of defects can be observed (Figure 2g). Figure S9 (Supporting Information) shows the photographic images of the calcium film encapsulated with different barrier films, and the evolution of the remaining area versus aging times is shown in Figure 2h. As seen here, after CYTOP coating, the corrosion of calcium film was significantly slowed down. Different from the sporadic corrosion of calcium film protected by 3CON film, the corrosion of calcium thin film protected by CON/CYTOP main due to the edge penetration, indicating a significantly improved water vapor barrier capability. WVTRs of these films were then calculated according to Equation 1, and these results are shown in Figure 2i. In comparison to the CYTOP-free films (vide supra), the CYTOP-containing one- and three-coupled CON films showed low WVTRs of 5.2×10^{-2} and 1.0×10^{-2} g m^{-2} d^{-1}, respectively, which is two orders of magnitude improved. Note that CYTOP thin film showed a poor WVTR of 10 g m^{-2} d^{-1} (Figure 2i), such a water vapor blocking effect of CYTOP layer is rather due to the pinhole filling and the hydrophobic surface of the CYTOP coating layer than the barrier capability of CYTOP film. The protective effect of the organic outer layer on barrier films was also demonstrated in the study by Wang et al.[48] It is also worth noting that the MeOH vapor treatment still showed a positive effect in improving the water vapor barrier behavior. As shown in Figure 2i, the 3-CON/CYTOP film with MeOH treatment showed lower WVTR than the film without MeOH treatment, reaching 8.7×10^{-4} g m^{-2} d^{-1}, which meets the encapsulation requirements of OPVs.[28,45] The TEM cross-sectional view of the final optimized 3-CON(MeOH)/CYTOP film (Figure S10, Supporting Information) shows a stacked multilayered structure with a total thickness of 0.6 μm.

2.3. In Situ Deposition of the Barrier Films on High-Performance Organic Solar Cells

To demonstrate the practical applicability of these barrier films in OPV, high-performance polymer solar cells were fabricated and 3-CON(MeOH)/CYTOP films were deposited in situ on the cell surface. The schematic diagram and the photographs of the real cells are shown in **Figure 3**a,b, respectively. Note that the encapsulation films were prepared inside a N_2-filled glovebox according to the optimized method described above, and the processing temperature for the deposition of the barrier film was limited to 60 °C, ensuring excellent compatibility with OPVs. To ensure a good contact for *J-V* measurement, conductive silver paste was applied on the electrode before depositing the barrier films. Due to the protection of the aluminum electrode and the weak penetration of the 172 nm UV light, the damage to the device caused by the VUV light is negligible. At the same time, a water-cooling system is installed on the lamp to avoid the heating damage to the device by the prolonged exposure of the VUV light. Figure 3c,e shows the *J-V* characteristics of PM6:Y6 and PM6:L8-BO solar cells with an inverted structure of ITO/ZnO/BHJ/MoO_3/Al (see Figure S11, Supporting Information for the chemical structures of PM6, Y6 and L8-BO). As seen here, the PM6:Y6 and PM6:L8-BO cells before encapsulation showed high power conversion efficiencies (PCEs) of 15.19% and 17.28%, respectively, which are comparable to the results reported in the literature with the same device structure.[58,59] After the deposition of 3-CON(MeOH)/CYTOP encapsulation layer, almost no PCE decay was achieved, indicating excellent compatibility of the solution-processed in situ encapsulation method to OPVs.

The PM6:Y6 and PM6:L8-BO cells encapsulated with 3-CON(MeOH)/CYTOP barrier film were then aged at 25 °C/50% RH in a climate chamber. For comparison, solar cells without encapsulation were also fabricated and aged in the same chamber. Figure 3d,f shows the evolution of PCE over aging times (see photovoltaic parameters in Table S1 in supporting information). As seen here, the unencapsulated PM6:Y6 cells showed a significant PCE decay to ≈60% of its initial PCE in 50 h, while the encapsulated cells maintained 95% of its initial efficiency after aging for 960 h. Similarly, the encapsulated PM6:L8-BO cells kept a high PCE of more than 95% of its initial efficiency, while an obvious PCE decay of over 30% decay after aging for 100 h was exhibited for the encapsulation-free cells. The stability of the encapsulated devices in air are comparable to the stability of the unencapsulated devices in N_2-filled glovebox (Figure S12, Supporting Information). The excellent long-term stability of the encapsulated OPVs in a humid environment proves that we have successfully developed an effective method of encapsulating OPV devices that is compatible for in situ encapsulation of the cells with a solution process. Figure S13 (Supporting Information) shows the record lifetimes of encapsulated OPVs, the stability of high efficiency cells reported in this work is highly remarkable in this field.

We further tested the reliability of the in situ encapsulated OPVs under simulated heavy rainfall weather. Here we chose

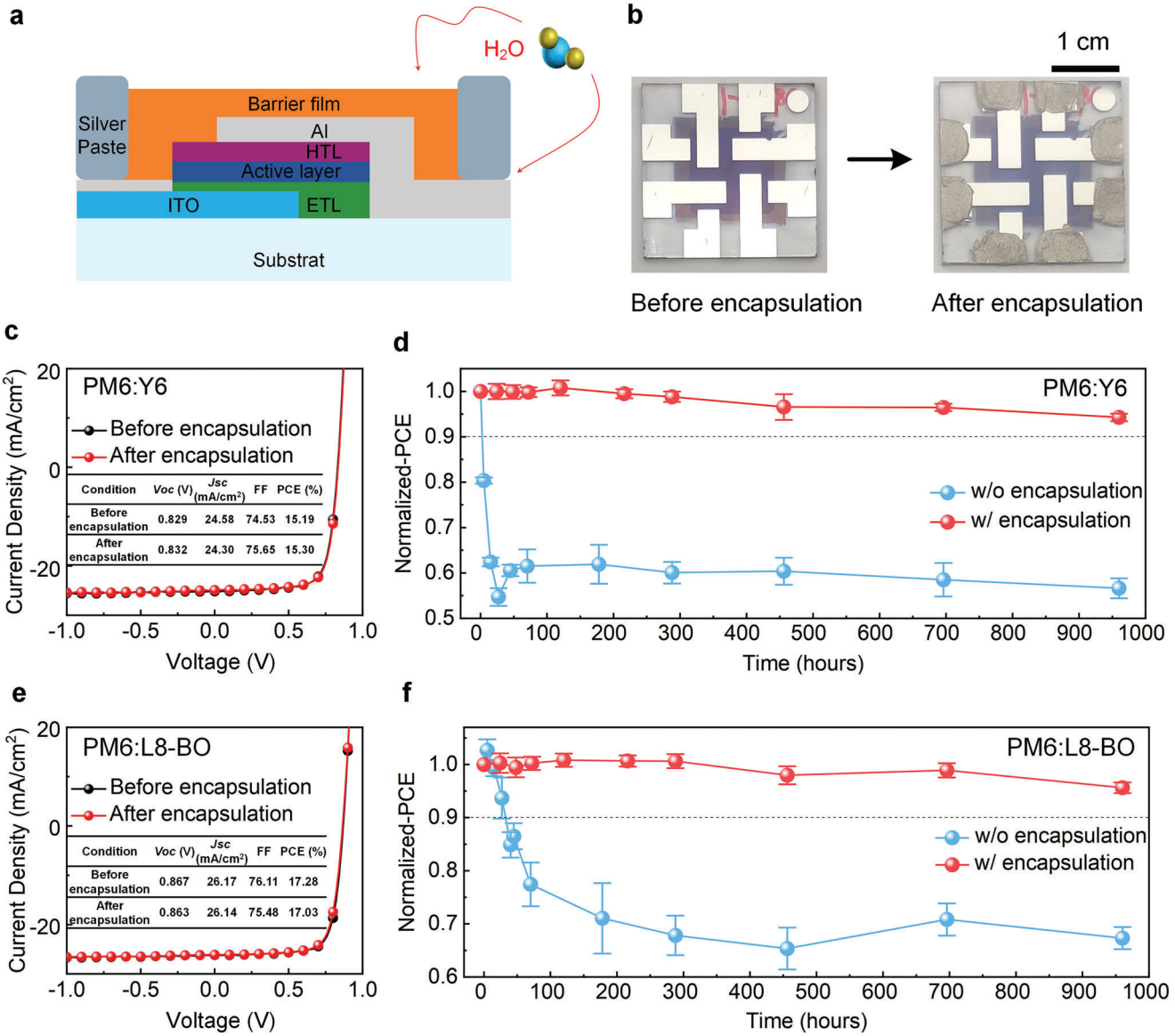

Figure 3. Solution-processed in situ encapsulation for OPVs and the stability test. a) Schematic diagram of encapsulated solar cell with an inverted structure of ITO/ZnO/BHJ/MoO_3/Al; b) Photographs of OPVs before and after in situ encapsulation; c,e) *J-V* curves of the inverted PM6:Y6 (c) and PM6:L8-BO (e) cells before and after encapsulation; d,f) Normalized efficiency decay curves of PM6:Y6 (d) and PM6:L8-BO (f) cells aged at 25 °C/50% RH.

inverted structure PM6:Y6 cells for the test. **Figure 4**a shows the testing set up, where the encapsulated OPVs were put directly under a shower with an angle of 45° with the encapsulation side facing the shower. The precipitation was controlled to be 50 mm h^{-1}, corresponding to a heavy rainstorm.[60] The OPVs were drenched with rain for 4 h and dried in ambient air for 8 h. The *J-V* characteristic was measured after such a rain-dry cycle. The photographs and the efficiency stability results are shown in Figure 4b,c. No photovoltaic performance data was measured after a heavy rain for two hours for the unencapsulated cell. Visual inspection indicates that some of the Al electrode was shed together with the MoO_3 layer, indicating that the weaker bonding between the MoO_3 layer and the electrode caused by rain is the main reason for the electrode shed. The cells encapsulated with 3-CON film failed in one test cycle. Although no electrode shedding was found, bumping of electrode was measured (Figure 4b), which can be ascribed to the unbalanced internal stress between the cell and the barrier film originating from the incomplete conversion of PDSN film (vide supra). In contrast, the cells encapsulated with the optimized barrier film maintained an initial efficiency of ≈90% after 8 testing cycles. These results demonstrate that the solution-processed in situ encapsulation method we developed could significantly improve the reliability of the polymer solar cells again with moisture penetration and heavy rain.

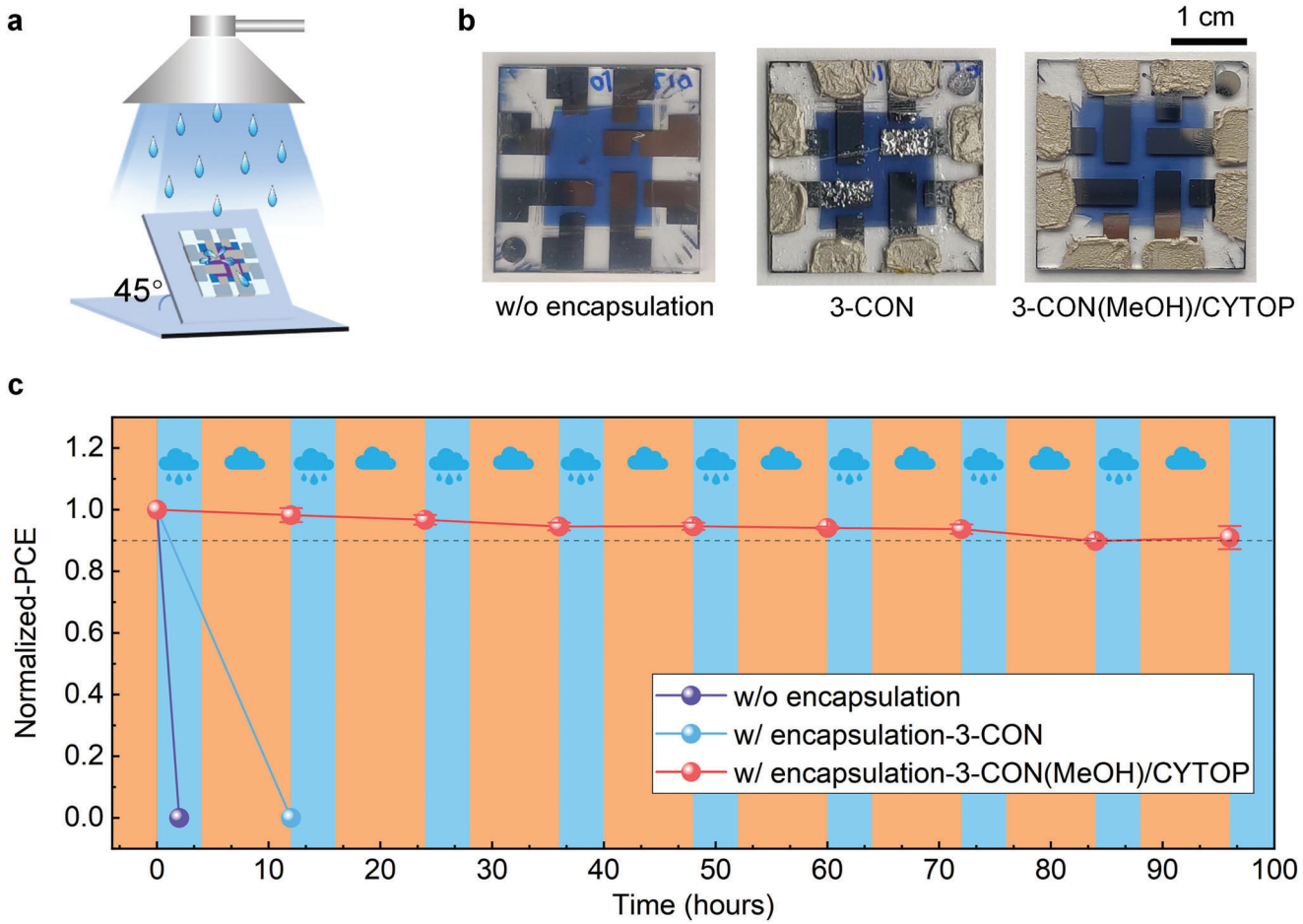

Figure 4. Reliability test of the solution-processed in situ encapsulated OPVs under heavy rain showering. a) Schematic diagram of the reliability test under a simulated rainstorm; b) Photographs of the cells with different encapsulation structure after one test cycle; c) Normalized efficiency changes of the inverted PM6:Y6 cells under the simulated rainstorm test cycle.

3. Conclusion

In summary, we have developed and optimized a solution-based process for the preparation of multilayered barrier films for in situ encapsulation of OPVs. Polysilicone and perhydropolysilianze (PHPS) were chosen as the precursor for the preparation of polymeric and inorganic layers, respectively, where both the polymer and the inorganic layers were densified with 172 nm VUV light irradiation. VUV-assisted conversion of PHPS to amorphous silicon nitride (PDSN) was confirmed by FTIR and TEM measurement and multilayered SiO_xC_y/a-SiN_x(O):H (shorted as CON) However, voids-like defects were found for the as-prepared PDSN film when it was exposed to the air, which was ascribed to the violent reaction of incomplete PDSN with moisture. MeOH vapor treatment was found to significantly improve the quality of the barrier film with decreasing the WVTR from 2.5 and 0.55 g m^{-2} d^{-1} to 0.5 and 0.2 g m^{-2} d^{-1} for the single CON and triple-CON films, respectively. Covering the CON surface with perfluoro polymer CYTOP can further decrease the WVTR to 5.2×10^{-2} g m^{-2} d^{-1} and 8.7×10^{-4} g m^{-2} d^{-1}, which was ascribed to the synergetic effect of void filling and hydrophobic surface effect. Application of this solution-processed barrier films in OPVs is carried out. Results showed that the deposition of the barrier films on OPV devices does not cause performance decay, whereas with the optimized barrier film (3CON-MeOH/CYTOP), the high-performance PM6:Y6 and PM6:L8-BO can maintain over 95% of its initial device performance at 25 °C/50% RH for 960 h, and can keep over 90% of its initial efficiency after 8 cycles of simulated rainstorm (50 mm h^{-1} for 4 h) and drying (for 8 h). The current work provides a feasible and applicable in situ thin film encapsulation method for air sensitive polymer solar cells.

Supporting Information

Supporting Information is available from the Wiley Online Library or from the author.

Acknowledgements

This work was supported by International Postdoctoral Exchange Fellowship Program (YJ20220152), the National Natural Science Foundation of China (22075315, 22022205), and Chinese Academy of Sciences (121E32KYSB20190021, YJKYYQ20180029).

Conflict of Interest

The authors declare no conflict of interest.

Data Availability Statement

The data that support the findings of this study are available from the corresponding author upon reasonable request.

Keywords

barrier films, organic photovoltaics, polymer-derived ceramics, solution process, thin film encapsulation

Received: March 1, 2023
Revised: March 22, 2023
Published online:

[1] N. Oreskes, *Science* **2004**, *306*, 1686.
[2] G.-R. Walther, E. Post, P. Convey, A. Menzel, C. Parmesan, T. J. C. Beebee, J.-M. Fromentin, O. Hoegh-Guldberg, F. Bairlein, *Nature* **2002**, *416*, 389.
[3] M. Chhowalla, H. S. Shin, G. Eda, L.-J. Li, K. P. Loh, H. Zhang, *Nat. Chem.* **2013**, *5*, 263.
[4] S. Chu, A. Majumdar, *Nature* **2012**, *488*, 294.
[5] D. Kraemer, B. Poudel, H.-P. Feng, J. C. Caylor, B. Yu, X. Yan, Y. Ma, X. Wang, D. Wang, A. Muto, K. McEnaney, M. Chiesa, Z. Ren, G. Chen, *Nat. Mater.* **2011**, *10*, 532.
[6] S. C. Roy, O. K. Varghese, M. Paulose, C. A. Grimes, *ACS Nano* **2010**, *4*, 1259.
[7] W. C. Sinke, M. M. Wienk, *Nature* **1998**, *395*, 544.
[8] G. Hodes, *Science* **2013**, *342*, 317.
[9] I. Burgues-Ceballos, L. Lucera, P. Tiwana, K. Ocytko, L. W. Tan, S. Kowalski, J. Snow, A. Pron, H. Burckstummer, N. Blouin, G. Morse, *Joule* **2021**, *5*, 2261.
[10] Y.-B. Cheng, A. Pascoe, F. Huang, Y. Peng, *Nature* **2016**, *539*, 488.
[11] Y. Li, G. Xu, C. Cui, Y. Li, *Adv. Energy Mater.* **2018**, *8*, 1701791.
[12] B. Shi, L. Duan, Y. Zhao, J. Luo, X. Zhang, *Adv. Mater.* **2020**, *32*, 1806474.
[13] C. J. Brabec, A. Distler, X. Du, H.-J. Egelhaaf, J. Hauch, T. Heumueller, N. Li, *Adv. Energy Mater.* **2020**, *10*, 2001864.
[14] R. Sun, T. Wang, X. R. Yang, Y. Wu, Y. Wang, Q. Wu, M. J. Zhang, C. J. Brabec, Y. F. Li, J. Min, *Nat. Energy* **2022**, *7*, 1087.
[15] Y. Cui, Y. Xu, H. Yao, P. Bi, L. Hong, J. Zhang, Y. Zu, T. Zhang, J. Qin, J. Ren, Z. Chen, C. He, X. Hao, Z. Wei, J. Hou, *Adv. Mater.* **2021**, *33*, 2102420.
[16] K. Jiang, J. Zhang, C. Zhong, F. R. Lin, F. Qi, Q. Li, Z. X. Peng, W. Kaminsky, S. H. Jang, J. W. Yu, X. Deng, H. W. Hu, D. Shen, F. Gao, H. Ade, M. Xiao, C. F. Zhang, A. K. Y. Jen, *Nat. Energy* **2022**, *7*, 1076.
[17] L. Zhu, M. Zhang, J. Xu, C. Li, J. Yan, G. Zhou, W. Zhong, T. Hao, J. Song, X. Xue, Z. Zhou, R. Zeng, H. Zhu, C.-C. Chen, R. C. I. MacKenzie, Y. Zou, J. Nelson, Y. Zhang, Y. Sun, F. Liu, *Nat. Mater.* **2022**, *21*, 656.
[18] L. Duan, A. Uddin, *Adv. Sci.* **2020**, *7*, 1903259.
[19] M. Jorgensen, K. Norrman, F. C. Krebs, *Sol. Energy Mater. Sol. Cells* **2008**, *92*, 686.
[20] M. Wang, F. Xie, J. Du, Q. Tang, S. Zheng, Q. Miao, J. Chen, N. Zhao, J. B. Xu, *Sol. Energy Mater. Sol. Cells* **2011**, *95*, 3303.
[21] T. S. Glen, N. W. Scarratt, H. Yi, A. Iraqi, T. Wang, J. Kingsley, A. R. Buckley, D. G. Lidzey, A. M. Donald, *Sol. Energy Mater. Sol. Cells* **2015**, *140*, 25.
[22] Y. Liang, D. Zhang, Z. Wu, T. Jia, L. Lüer, H. Tang, L. Hong, J. Zhang, K. Zhang, C. J. Brabec, N. Li, F. Huang, *Nat. Energy* **2022**, *7*, 1180.
[23] Y. Li, X. Huang, K. Ding, H. K. M. Sheriff Jr., L. Ye, H. Liu, C.-Z. Li, H. Ade, S. R. Forrest, *Nat. Commun.* **2021**, *12*, 5419.
[24] Y. Han, Z. Hu, W. Zha, X. Chen, L. Yin, J. Guo, Z. Li, Q. Luo, W. Su, C.-Q. Ma, *Adv. Mater.* **2022**, *34*, 2110276.
[25] R. Sun, T. Wang, Y. Wu, M. Zhang, Y. Ma, Z. Xiao, G. Lu, L. Ding, Q. Zheng, C. J. Brabec, Y. Li, J. Min, *Adv. Funct. Mater.* **2021**, *31*, 2106846.
[26] Y. Wang, Z. Zheng, J. Wang, X. Liu, J. Ren, C. An, S. Zhang, J. Hou, *Adv. Mater.* **2022**, 2208305.
[27] M. Cui, D. Li, X. Du, N. Li, Q. Rong, N. Li, L. Shui, G. Zhou, X. Wang, C. J. Brabec, L. Nian, *Adv. Mater.* **2020**, *32*, 2002973.
[28] J. Ahmad, K. Bazaka, L. J. Anderson, R. D. White, M. V. Jacob, *Renewable Sustainable Energy Rev.* **2013**, *27*, 104.
[29] H. C. Weerasinghe, S. E. Watkins, N. Duffy, D. J. Jones, A. D. Scully, *Sol. Energy Mater. Sol. Cells* **2015**, *132*, 485.
[30] A. Kovrov, M. Helgesen, C. Boeffel, S. Kropke, R. R. Sondergaard, *Sol. Energy Mater. Sol. Cells* **2020**, *204*, 110210.
[31] M. Giannouli, V. M. Drakonakis, A. Savva, P. Eleftheriou, G. Florides, S. A. Choulis, *ChemPhysChem* **2015**, *16*, 1134.
[32] I. A. Channa, A. Distler, C. J. Brabec, H.-J. Egelhaaf, in *Organic Flexible Electronics*, Woodhead Publishing, Cambridge **2021**, p. 249.
[33] E. G. Jeong, J. H. Kwon, K. S. Kang, S. Y. Jeong, K. C. Choi, *J. Inf. Disp.* **2020**, *21*, 19.
[34] S. Lee, J.-H. Han, S.-H. Lee, G.-H. Baek, J.-S. Park, *JOM* **2018**, *71*, 197.
[35] A. Uddin, M. B. Upama, H. Yi, L. Duan, *Coatings* **2019**, *9*, 65.
[36] K. Y. Lim, H. H. Kim, J. H. Noh, S. H. Tak, J.-W. Yu, W. K. Choi, *RSC Adv.* **2022**, *12*, 4113.
[37] J. H. Kwon, Y. Jeon, S. Choi, J. W. Park, H. Kim, K. C. Choi, *ACS Appl. Mater. Interfaces* **2017**, *9*, 43983.
[38] F. Bauer, U. Decker, A. Dierdorf, H. Ernst, R. Heller, H. Liebe, R. Mehnert, *Prog. Org. Coat.* **2005**, *53*, 183.
[39] L. Prager, A. Dierdorf, H. Liebe, S. Naumov, S. Stojanovic, R. Heller, L. Wennrich, M. R. Buchmeiser, *Chem. - Eur. J.* **2007**, *13*, 8522.
[40] J. S. Lee, J. H. Oh, S. W. Moon, W. S. Sul, S. D. Kim, *Electrochem. Solid-State Lett.* **2010**, *13*, H23.
[41] Y. Kobayashi, H. Yokota, Y. Fuchita, A. Takahashi, Y. Sugahara, *J. Ceram. Soc. Jpn.* **2013**, *121*, 215.
[42] N. Shinde, Y. Takano, J. Sagan, V. Monreal, T. Nagahara, *J. Photopolym. Sci. Technol.* **2010**, *23*, 225.
[43] A. Morlier, S. Cros, J.-P. Garandet, N. Alberola, *Sol. Energy Mater. Sol. Cells* **2013**, *115*, 93.
[44] L. Prager, L. Wennrich, R. Heller, W. Knolle, S. Naumovll, A. Prager, D. Decker, H. Liebe, M. R. Buchmeiser, *Chem. - Eur. J.* **2009**, *15*, 675.
[45] I. A. Channa, A. Distler, M. Zaiser, C. J. Brabec, H.-J. Egelhaaf, *Adv. Energy Mater.* **2019**, *9*, 1900598.
[46] L. Sun, K. Uemura, T. Takahashi, T. Yoshida, Y. Suzuri, *ACS Appl. Mater. Interfaces* **2019**, *11*, 43425.
[47] J. Kim, H.-J. Song, C. Lee, *Energies* **2021**, *14*, 3993.
[48] L. Wang, C. Ruan, M. Li, J. Zou, H. Tao, J. Peng, M. Xu, *J. Mater. Chem. C* **2017**, *5*, 4017.
[49] T. Sasaki, L. Sun, Y. Kurosawa, T. Takahashi, Y. Suzuri, *Adv. Mater. Interfaces* **2022**, *9*, 2201517.
[50] L. Sun, Y. Kurosawa, H. Ito, Y. Makishima, H. Kita, T. Yoshida, Y. Suzuri, *Org. Electron.* **2019**, *64*, 176.
[51] T. Sasaki, L. N. Sun, Y. Kurosawa, T. Takahashi, Y. Suzuri, A. C. S. Appl, *Nano Mater* **2021**, *4*, 10344.
[52] J. J. Baek, S. M. Park, Y. R. Kim, K. C. Chang, Y.-J. Heo, G. Y. Bae, K. H. Choi, G. Shin, *J. Mater. Sci.* **2022**, *57*, 254.
[53] M. S. Weaver, L. A. Michalski, K. Rajan, M. A. Rothman, J. A. Silvernail, J. J. Brown, P. E. Burrows, G. L. Graff, M. E. Gross, P. M. Martin, M.

Hall, E. Mast, C. Bonham, W. Bennett, M. Zumhoff, *Appl. Phys. Lett.* **2002**, *81*, 2929.
[54] O. Zhao, Y. Ding, Z. Pan, N. Rolston, J. Zhang, R. H. Dauskardt, *ACS Appl. Mater. Interfaces* **2020**, *12*, 26405.
[55] A. B. Schroeder, E. T. A. Dobson, C. T. Rueden, P. Tomancak, F. Jug, K. W. Eliceiri, *Protein Sci.* **2021**, *30*, 234.
[56] D. Wang, X. Guo, P. F. Li, Y. L. Zhang, C. H. Xu, Z. B. Zhang, *Acta Chim. Sinica* **2022**, *80*, 734.
[57] Y. Li, K. Cao, Y. F. Xiong, H. Yang, Y. Zhang, Y. Lin, B. Zhou, J. Huang, R. Chen, *Adv. Mater. Interfaces* **2020**, *7*, 2000237.
[58] L. Hong, H. Yao, Y. Cui, R. Yu, Y.-W. Lin, T.-W. Chen, Y. Xu, J. Qin, C.-S. Hsu, Z. Ge, J. Hou, *Small* **2021**, *17*, 2101133.
[59] B. Liu, X. Su, Y. Lin, Z. Li, L. Yan, Y. Han, Q. Luo, J. Fang, S. Yang, H. Tan, C.-Q. Ma, *Adv. Sci.* **2022**, *9*, 2104588.
[60] Y. Jiang, L. Qiu, E. J. Juarez-Perez, L. K. Ono, Z. Hu, Z. Liu, Z. Wu, L. Meng, Q. Wang, Y. Qi, *Nat. Energy* **2019**, *4*, 585.